Energy 318 (2025) 134731

Contents lists available at ScienceDirect

Energy

journal homepage: www.elsevier.com/locate/energy

Thermal design framework of heat pipe heat exchanger for efficient waste heat recovery

Seungjae Lee [a], Sukkyung Kang [b], Yunseo Kim [a], Gyohoon Geum [c], Daeyoung Kong [d], Dong Hwan Shin [e], Seong Hyuk Lee [a,c], Jungho Lee [b,1,*], Hyoungsoon Lee [a,c,2,**]

[a] School of Mechanical Engineering, Chung-Ang University, Seoul 06974, South Korea
[b] Department of Mechanical Engineering, Ajou University, Suwon, Gyeonggi-do 16499, South Korea
[c] Department of Intelligent Energy and Industry, Chung-Ang University, Seoul 06974, South Korea
[d] Department of Mechanical Engineering, Stanford University, CA 94305, USA
[e] Department of Thermal Energy Solutions, Korea Institute of Machinery & Materials, Daejeon 34103, South Korea

ARTICLE INFO

Keywords:
Waste heat recovery
Porous media model
Local thermal nonequilibrium model

ABSTRACT

Recovering waste heat efficiently is crucial to addressing global energy challenges and mitigating climate change, positioning heat pipe heat exchangers (HPHXs) as a promising solution. However, the computational modeling of HPHXs, particularly for finned configurations, remains challenging due to high computational costs. Consequently, existing research predominantly focuses on unfinned heat exchangers, while the performance of finned designs is typically estimated using empirical correlations or experimental data. Comprehensive analyses of finned HPHXs undergoing phase changes remain scarce. This study addresses these challenges by introducing a thermal design framework that approximates heat pipes as solid conductors with effective thermal conductivity and models finned sections as porous media. This innovative framework not only streamlines computational modeling but also enables accurate thermal performance predictions without reliance on experimental data. Using the proposed framework, HPHXs were modeled with 95 copper two-phase closed thermosyphons (TPCTs) and baffles, providing precise thermal performance analysis. To validate the framework, a full-scale HPHX test module was developed and experimentally tested. The model successfully predicted the performance of an HPHX recovering 30.2 kW of waste heat, achieving a thermal effectiveness of 0.78 and predictive accuracy within ±6.2 % of the measured energy recovery rate. This research establishes a reliable and scalable methodology for designing efficient HPHXs, representing a significant advancement in industrial waste heat recovery systems.

1. Introduction

Energy is a fundamental driver of human activities and development, making it a critical component in assessing the industrial economy. However, rapid population growth has accelerated the depletion of energy resources [1,2]. Over the past few decades, global energy demand has increased exponentially, increasing from 8588.9 million tonnes of oil equivalent (Mtoe) in 1995 to 13,147.3 Mtoe by 2015 [3]. This steady rise in energy consumption has been paralleled by an exponential increase in greenhouse gas emissions, presenting significant challenges in improving energy efficiency and mitigating environmental impact. In 2021, the Lawrence Livermore National Laboratory reported that the United States wasted 65.4 quads (6.5×10^{16} Btu) of energy, accounting for ~67 % of its total energy consumption of 97.3 quads (10.3×10^{16} Btu) [4]. This energy waste is largely attributed to the inefficiencies in the conversion of raw materials into useable energy, resulting in substantial losses during energy conversion processes. Research by Cullen and Allwood found that roughly 63 % of the world's primary energy is lost through combustion and heat transfer processes [5], with a significant portion discarded as waste heat [6]. Recovering and reusing waste heat presents an opportunity to achieve substantial energy savings, and enhance process efficiency, thereby addressing critical environmental challenges [7].

* Corresponding author at: Department of Mechanical Engineering, Ajou University, Suwan, Gyeonggi-do 16499, South Korea.
** Corresponding author at: School ofMechanical Engineering, Chung-Ang University, Seoul 06974, South Korea.
E-mail addresses: jungholee@ajou.ac.kr (J. Lee), leeh@cau.ac.kr (H. Lee).
[1] http://atmlab.ajou.ac.kr/
[2] http://atsla.cau.ac.kr

https://doi.org/10.1016/j.energy.2025.134731
Received 3 October 2024; Received in revised form 20 January 2025; Accepted 24 January 2025
Available online 28 January 2025
0360-5442/

Nomenclature

A	area [mm^2]
a	fitting coefficient
b	fitting coefficient
C	heat capacity rate [W/K]
C_1	viscous resistance coefficient
C_2	inertial resistance coefficient
$C_{i,j}$	inertial loss coefficient matrix
c_p	specific heat [J/kg·K]
D_o	heat pipe outer diameter [mm]
D_c	condenser inlet–outlet diameter [mm]
D_e	evaporator inlet–outlet diameter [mm]
$D_{i,j}$	viscous loss coefficient matrix
H	height [mm]
h	heat transfer coefficient [$W/m^2 \cdot K$]
k	thermal conductivity [W/m·K]
Δn	porous media thickness [m]
L	length [mm]
$\dot{m}$	mass flow rate [kg/s]
Q	heat transfer rate [W]
S_i	momentum source term in the ith direction [$kg/(m^2 \cdot s^2)$]
S_T	transverse spacing [mm]
S_L	longitudinal spacing [mm]
T	temperature [°C]
t	thickness [mm]
u	fluid velocity [m/s]
W	width [mm]

Greek symbols

Δ	difference
α	permeability [m^2]
ε	effectiveness
μ	dynamic viscosity [kg/m·s]
ρ	density [kg/m^3]

Subscripts

air	air
c	condenser
e	evaporator
eff	effective
in	inlet
max	maximum
min	minimum
out	outlet
w	water
wall	wall

HPHXs transfer heat from high-temperature sources to low-temperature sinks through the phase change of working fluid, alternating between liquid and vapor states [8]. This phase-change mechanism allows HPHXs to operate efficiently even with small temperature differentials while exhibiting excellent resistance to thermal deformation. Additionally, their straightforward design ensures easy maintenance, making them a reliable choice for industrial applications. Because of these advantages, HPHXs are widely employed for waste heat recovery in various sectors, including steel production [9], petrochemical and chemical industries, power generation, construction materials [10,11], automotive manufacturing [12], and air-conditioning systems [13,14].

To develop efficient heat exchangers for waste heat recovery in industrial applications, it is essential to understand and accurately predict the impact of geometric design and operating conditions on heat and fluid performance. However, experimentally analyzing these parameters can be both time-consuming and costly due to the complexity of heat transfer, which is influenced by various parameters. Several researchers have developed empirical models to assess the performance of HPHXs. For example, Longo et al. [15] and Jouhara et al. [16] utilized the widely recognized log mean temperature difference (LMTD) method to evaluate the thermal performance of HPHXs, with their results closely matching experimental data. Additionally, the ε-NTU approach is commonly used for evaluating heat exchanger efficiency and has been applied in numerous studies [17,18] to assess HPHX performance. However, these empirical models often struggle to accurately predict the behavior of new systems or conditions that lack sufficient and diverse data. To overcome these limitations, computational analysis has been increasingly employed to evaluate the thermal heat and fluid performance of heat exchangers. This approach aims to enhance prediction accuracy, optimize geometries, and reduce computational costs. Mrooue et al. [19] used a thermal network model of a two-phase closed thermosyphon (TPCT) to investigate phase change phenomena in heat pipe components, yielding predictions that closely aligned with experimental data, with a margin of error less than 10 %. Cho et al. [20] developed a model based on mass balance and operational saturation points to accurately predict TPCT behavior, with a maximum deviation of just 6 % compared to experimental results. Brough et al. [21] conducted a full-scale HPHX simulation using a TRNSYS-based computational model, reporting exceptional prediction accuracy within ±4 % of experimental results for heat recovery from exhaust gases in a ceramic kiln system. Selma et al. [22] developed a simulation in OpenFOAM to analyze a finned HPHX used in HVAC systems for waste heat recovery. Their study focused on optimizing geometry by analyzing fluid flow and thermal performance, leading to a 24 % improvement in performance and a 30 % reduction in pressure drop. Similarly, Geum et al. [23] computationally optimized HPHX geometries and experimentally verified a heat recovery rate of 19.7 kW from hot air flow.

Several studies have focused on minimizing computational costs while enhancing prediction accuracy for complex HPHX systems. Ramos et al. [24] treated heat pipes as solid conductors with high thermal conductivity, achieving accurate predictions of heat transfer rates and efficiency within an error margin of just 10 %. Varol et al. [25] employed two-dimensional symmetric computational domains to reduce computation time for HPHX systems with smooth internal tubes. Lindqvist and Näss [26] introduced a computational domain that utilized geometric periodicity, simplifying calculations for the heat-hydraulic performance of finned tube bundles. To further reduce computational costs, several studies have applied the porous media model. Qu et al. used this model to analyze a finned oval tube heat exchanger [27]. Guler [28] applied a porous media model in ANSYS Fluent to analyze the thermal performance of vehicle radiators, treating a section of the radiator as a unit cell with periodicity. This approach yielded a 2.5 % error in outlet temperature predictions. Gangapatnam and Priyatham [29] conducted a numerical study on forced convection heat transfer within high-porosity aluminum foam, using the porous media model. Their local thermal non-equilibrium (LTNE) model matched experimental results with an error of 15 %. A.M. Hayes and Jamil A. Khan [30] employed the porous media model and LTNE for a matrix heat exchanger, obtaining the heat transfer coefficient (HTC) from a numerical model based on experimental data. Their uncertainty analysis, using the Kline–McClintock method, revealed a 2.7 % error in the calculated HTC.

Before the fabrication of heat exchangers, validation through computational fluid dynamics (CFD) is essential, as it significantly reduces time and costs compared to experimental testing. However, many studies simplify simulations by assuming thermal equilibrium in porous media, which can compromise accuracy in systems with complex geometries and diverse operating conditions. While thermal non-equilibrium models provide greater precision, they often depend on empirical correlations and experimental data, creating challenges in accurately modeling finned HPHXs. This highlights the need for a robust analytical approach capable of modeling heat exchangers with numerous fins effectively. This study introduces a thermal design framework to address the challenges of accurately modeling thermal non-equilibrium in HPHXs. The approach employs unit cell models to characterize flow resistance and heat transfer rates within porous media, enabling precise predictions of HPHX thermal performance. The framework was validated through experimental testing under various flow conditions, where it demonstrated superior accuracy and reliability compared to conventional thermal equilibrium analyses. A key advantage of the proposed framework is its ability to deliver accurate predictions for complex geometries without relying on empirical correlations or extensive experimental data. This capability significantly reduces computational costs and eliminates the need for empirical tuning. By streamlining simulations, the framework enables faster and more cost-effective optimization of HPHX designs, enhancing thermal performance while minimizing resource consumption.

Although this study focuses on the fundamental development of heat exchangers for waste heat recovery, the findings offer valuable insights for optimizing the geometric design of HPHX systems across a range of applications, including gas turbine exhaust, steel heat treatment, and organic chemical processing [31].

2. Computational model

A full-scale conjugate simulation of fluid flow and heat transfer was performed to predict the thermal performance of an HPHX. The HPHX was equipped with 95 finned heat pipes to enhance heat transfer from the evaporator to the condenser. Each heat pipe featured 115 circular copper fins designed to minimize convective thermal resistance. To optimize computational efficiency, a porous media model was applied to the finned areas. Additionally, two different heat transfer models (nonequilibrium and equilibrium) were implemented in the porous media zone to assess performance under varying conditions. The thermal design framework for the HPHX was developed through a systematic approach. First, flow resistance was calibrated using unit cell simulations that simplified the complex fin geometry. Then, the heat transfer coefficient within the porous media was determined by comparing heat transfer rates between a finned tube and its porous media equivalent. These calibrated parameters were subsequently integrated into a full-scale model to simulate the thermal performance of the HPHX. Finally, the model's accuracy was validated by comparing its predictions with experimental data obtained from a constructed heat exchanger.

2.1. Full-scale conjugate simulation

Fig. 1 illustrates the geometry and boundary conditions used in this study for the HPHX. The base geometry was derived from the optimal shape determined in previous research by the authors [23]. It consists of a high-temperature evaporator section and a low-temperature condenser section. Air and water were used on the high-temperature evaporator and low-temperature condenser sides, respectively. As shown in Fig. 1(a), the dimensions of the HPHX were 540 mm (W) × 540 mm (L) × 445 mm (H). The inlet and outlet locations for the evaporator and condenser sections are depicted in Fig. 1(b) and (c), respectively. The air inlet and outlet had an internal diameter of 299.5 mm and were connected to the 300 mm high evaporator section on the high-temperature side. The water inlet and outlet, each with a diameter of 33.0 mm, were connected to the condenser section, which had a height of 125 mm and was positioned on the top of the HPHX. A 20-mm-thick separator, made from Al6061 (k = 167 W/m·K), was installed between the evaporator and condenser sections. To optimize

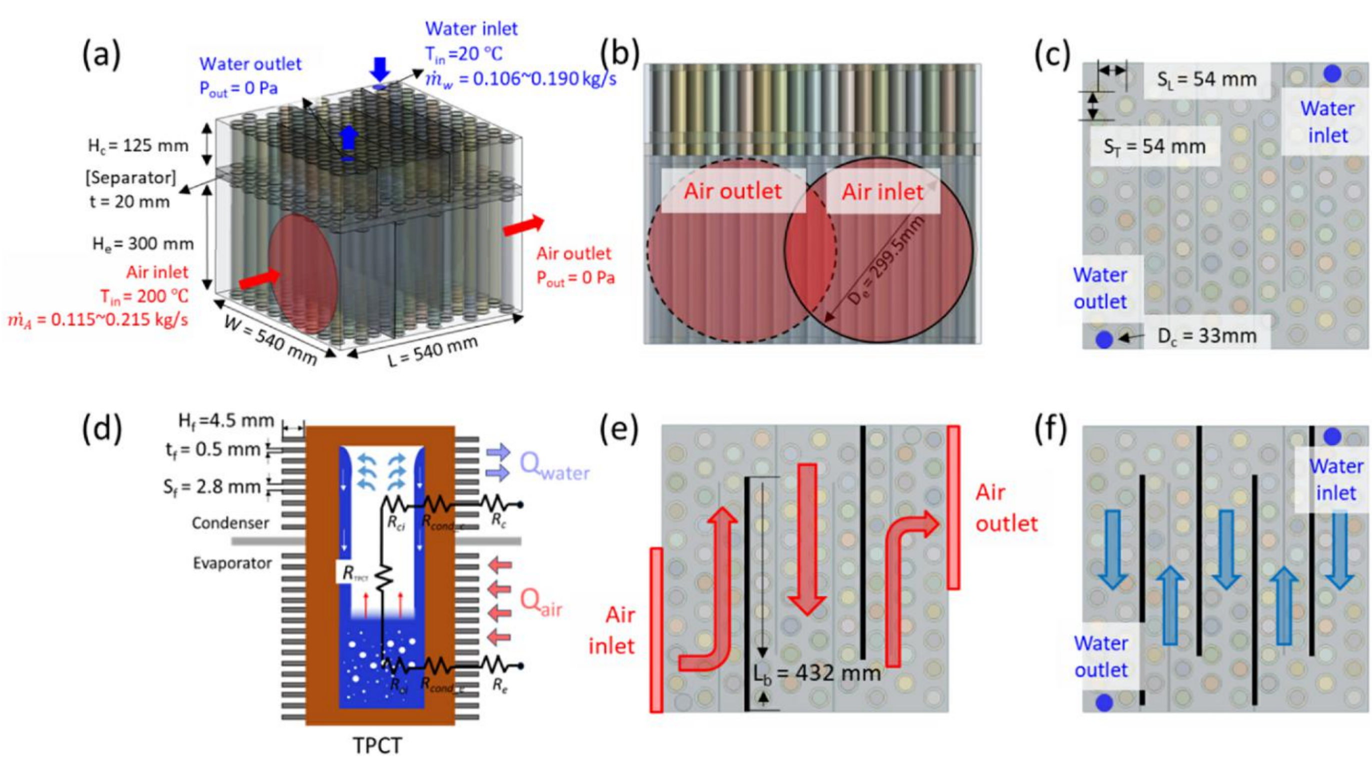

Fig. 1. | **Configuration of an HPHX.** (**a**) Schematic representation of the computational domain and its boundary conditions. (**b**) Diagrams of the geometry of the evaporator inlet and outlet (**b**) and the condenser inlet and outlet (**c**). (**d**) Configuration of the partial fins and heat transfer pathway. (**e-f**) Representative baffle designs in the evaporator (**e**) and condenser (**f**).

the contact area between the working fluid and the heat pipes, two baffles were installed in the evaporator section and four in the condenser section, each 2 mm thick. Additionally, to simplify the computational complexity of the phase change process within the heat pipes, a solid rod with an effective thermal conductivity of $k_{eff} = 65{,}000$ W/m·K replaced the heat pipe in the model [32]. The heat pipes themselves had a $D_o =$ 28.6 mm, each equipped with 115 fins. These fins had $t_f = 0.5$ mm, $H_f =$ 4.5 mm, and $S_f = 2.8$ mm. In the evaporator section, 85 fins were distributed along 278.5 mm of the total 300 mm length, while in the condenser section, 30 fins were installed along 99 mm of the 125 mm length. The 95 heat pipes were arranged with a center-to-center spacing ($S_T = S_L$) = of 54 mm within the HPHX.

The simulation was performed under steady-state conditions with incompressible fluid flow. The SIMPL algorithm was used to couple pressure and velocity, and a least-squares cell-based approach was applied for gradient discretization. A second-order scheme was employed for pressure discretization, while momentum and energy were discretized using a second-order upwind method. The k-ε realizable model was selected for the simulations due to its superior accuracy at higher Reynolds numbers and pressure gradients [33]. Convergence criteria were set to below 10^{-3} for the continuity equation, velocity components, k, and ε, and below 10^{-6} for the energy equation [34].

For the evaporator section, the inlet boundary condition was specified by mass flow rate and $T_{air,in} = 200$ °C. The condenser section used a mass flow rate condition at the inlet, with an inlet temperature $T_{w,in}$ set to 20 °C. Pressure outlet conditions were applied to both outlets. The no-slip condition, along with coupled boundary conditions, was imposed at all fluid-solid interfaces, while the remaining walls were treated as adiabatic.

Polyhedral meshing was adopted, and an inflation mesh with 10 layers and a growth rate of 1.2 was applied to all fluid-solid interfaces. Mesh independence tests were conducted, with a total element count reaching up to 65 million. The heat transfer rate variation remained within 1 % for meshes containing more than 39 million elements. Therefore, a mesh with 39 million elements was selected for all full-scale simulations to balance accuracy and computational cost. Detailed mesh independence test results are provided in Appendix A of the Supporting Information.

2.2. Porous media model approach

A porous media model was applied around the region containing 115 fins on each tube to accurately capture the thermofluidic behavior of the finned HPHX, significantly reducing computational costs. As shown in Fig. 2(a), the porous media zone spans 278.5 mm along a 300-mm tube in the evaporator section and 99 mm along a 125-mm tube in the condenser section. The application of the porous model involved two key steps: first, determining the flow resistance needed to predict fluid flow accurately within the porous media, and second, selecting an appropriate heat transfer model to calculate the heat transfer rate accurately. Both flow resistance and heat transfer coefficients for the finned HPHX were characterized using two distinct unit cell models.

2.2.1. Determination of flow resistance in the porous media model

To model the flow resistance induced by discrete pins, a momentum source term S_i is introduced on the right-hand side of the momentum equation in the porous media model. The momentum source term in the i-th direction is given by:

$$S_i = -\left(\sum_{j=1}^{3} D_{ij}\mu u_j + \sum_{j=1}^{3} C_{ij}\frac{1}{2}\rho|u|u_j\right). \tag{1}$$

The right-hand side of the equation represents the viscous loss and inertial loss, respectively. Here, D_{ij} and C_{ij} are the matrices for the viscous and inertial loss coefficients, respectively. For a simple homogeneous porous medium, the viscous loss coefficient D_{ij} simplifies to μ/α, and the inertial loss coefficient C_{ij} simplifies to C_2, where μ is the dynamic viscosity, α is the permeability of the medium, and C_2 is a constant that accounts for the inertial loss. Thus, the momentum source term can be written as follows:

$$S_i = -\left(\frac{\mu}{\alpha}u_i + C_2\frac{1}{2}\rho|u|u_i\right) = -\left(C_1\mu u_i + C_2\frac{1}{2}\rho|u|u_i\right), \tag{2}$$

where α denotes the permeability, C_1 represents the viscous resistance coefficient (defined as α^{-1}), and ρ is the fluid density. The pressure drop (ΔP) was obtained from unit cell simulations for inlet velocities ranging from 1 to 10 m/s, using air and water for the evaporator and condenser sections, respectively. The relationship between ΔP and velocity (u) was determined and can be expressed by the following equations [35]:

$$\Delta P = -S_i\Delta n = au^2 + bu, \tag{3}$$

where a and b are fitting coefficients, and Δn is the thickness of the porous media. By comparing Eqns. (2) and (3), the resistance coefficients and fitting coefficients a and b for the porous media can be written as follows:

$$a = \frac{1}{2}C_2\rho\Delta n, \tag{4a}$$

$$b = C_1\mu\Delta n. \tag{4b}$$

In the porous media model, Eqns. (4a) and (4b) are used to calculate the viscous and inertial resistance coefficients, respectively. For analysis, isotropic flow resistance was assumed. For air, the calculated viscous

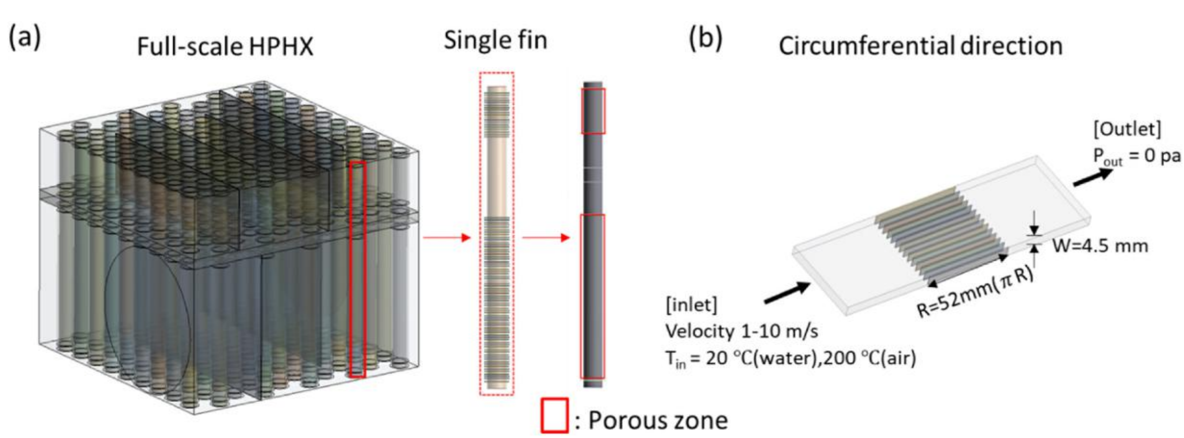

Fig. 2. | Porous media model approach in the HPHX. (**a**) Three-dimensional (3D) fin tube and 3D porous region. (**b**) Computational domain and boundary conditions used to determine the resistance coefficient in the porous media model.

resistance coefficient is 4.3×10^6, and the inertial resistance coefficient is 30.76. For water, the viscous resistance coefficient is 6.5×10^6, and the inertial resistance coefficient is 24.82.

2.2.2. Determination of heat transfer rate in the porous media model

Two distinct heat transfer models are employed to control the heat transfer rate in the porous media model: i) local thermal equilibrium (LTE) and ii) local thermal nonequilibrium. LTE assumes thermal equilibrium between the solid and liquid phases, eliminating the need for a separate HTC value. However, LTE tends to overestimate the heat transfer rate in porous media because it assumes ideal heat exchange with an infinitely high HTC between the solid and fluid phases, meaning two different temperatures can exist. To accurately calculate heat transfer within porous media using LTNE, an HTC between the solid and fluid phases must be specified.

The heat transfer coefficient in porous media was determined using a unit cell model, as illustrated in Fig. 3. The heat transfer rate was initially calculated for a model featuring fins on the tube. This rate was then compared to that of a model where the fins were replaced with porous media, allowing the appropriate HTC for the LTNE model to be determined. The unit cell analysis was performed on a single finned tube, placed 45 mm from the entrance and 205 mm from the exit to minimize any end effects. The same fin geometry (t_f, H_f, S_f) was used to obtain the heat transfer rate through the finned tube (Fig. 3(a)), while the finned area was substituted with porous media to calculate the heat transfer coefficient in porous media (Fig. 3(b)).

A velocity inlet boundary condition was applied for both air and water, with inlet temperatures set to 200 °C for air and 20 °C for water. A pressure outlet boundary condition was applied at the exit. In a typical fin-tube heat exchanger, the fluid velocity varies depending on the area through which the fluid flows. For the geometry in this study, the minimum velocity occurs at the inlet, while the maximum velocity appears between the transverse spacings of the tube. Based on this geometry, the velocity range was calculated, and the HTC (u) was determined to range from 6.63 to 10.27 m/s for air and 0.05–0.08 m/s for water. To account for the effects of multiple tube bank configurations within the heat exchanger, the HTC for a single tube was adjusted by applying a correction factor of 0.64 [36]. The resulting range of HTCs used in the LTNE model is provided in Table 1.

3. Experimental method

A full-scale HPHX test module was developed to experimentally validate the predictive accuracy of the proposed computational model. An open-loop system was constructed for testing, and experiments were conducted within the operational range defined in the analysis. Thermal and fluid characteristics were measured, and the accuracy of the computational analysis was confirmed through these experiments.

Table 1
| HTC as a function of flow rate.

Air mass flow rate [kg/s]	HTC_{air} [W/m^2·K]	Water mass flow rate [kg/s]	HTC_{water} [W/m^2·K]
0.115	271	0.106	5354
0.139	327	0.124	6264
0.165	389	0.143	7224
0.189	445	0.167	8436
0.215	506	0.190	9598

3.1. HPHX design and fabrication

Fig. 4(a) shows the heat pipe component, which was fabricated and tested to experimentally validate the HPHX. The dimensions of the TPCT and heat exchangers in the experimental setup were identical to those used in the numerical model. Water was selected as the working fluid for the TPCT, with a filling ratio of 35 %, based on an optimal value identified in a previous study [37]. Noncondensable gases were removed from the water using an induction heating method [38], which proved to be an efficient alternative to conventional vacuum-based techniques. Several TPCTs were simultaneously heated to 250 °C using ambient induction coils to ensure complete degassing by boiling the working fluid intensely. After the degassing period, the TPCTs were sealed using ultrasonic welding. Before production, 95 heat pipes were leak-tested using vacuum pumps to verify their airtightness. After the TPCTs were fabricated, their filling ratio was confirmed by measuring their weight.

Fig. 4(b) shows a photograph of the assembled HPHX. The cover of the HPHX was made from 5-mm stainless steel, while the evaporator and condenser were constructed from 20-mm-thick Al 6061. To manage the high flow rates of hot air and cold water, two baffles were installed in the evaporator and four in the condenser. These 2-mm stainless-steel baffles were welded to the HPHX enclosure. A silicone gasket was placed between the separation plate and the heat exchanger cover, while polytetrafluoroethylene tape was wrapped around the threaded sections of each finned heat pipe to prevent leakage.

3.2. Experimental setup and test conditions

Fig. 5 illustrates a flow loop designed to assess the thermal performance of the HPHX. To maintain a constant temperature of 200 °C at the evaporator inlet, the air was preheated using a 300 kW duct heater

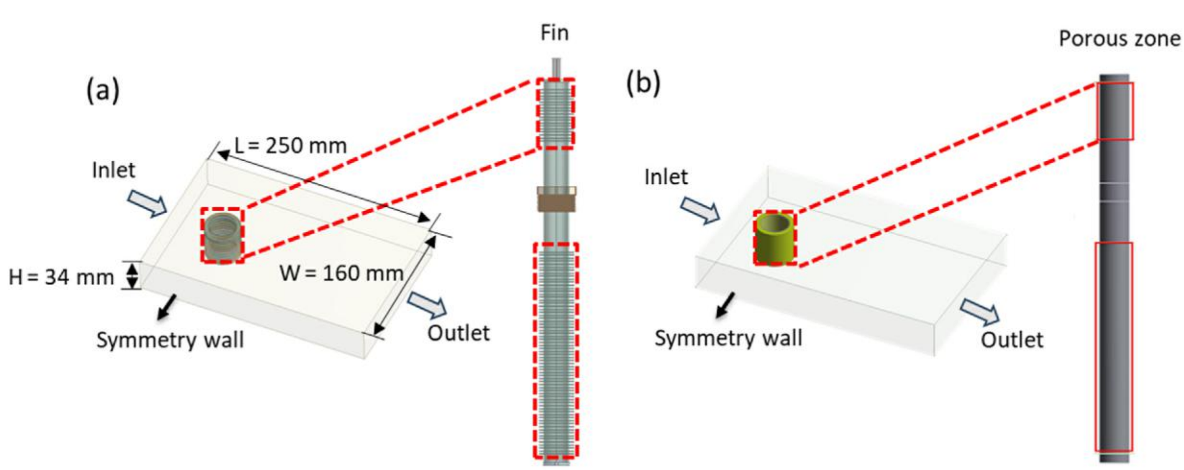

Fig. 3. | **Unit-cell analysis for determining heat transfer coefficients in a porous media model.** (**a**) A unit cell containing a finned tube. (**b**) A unit cell with the finned region is replaced by porous media.

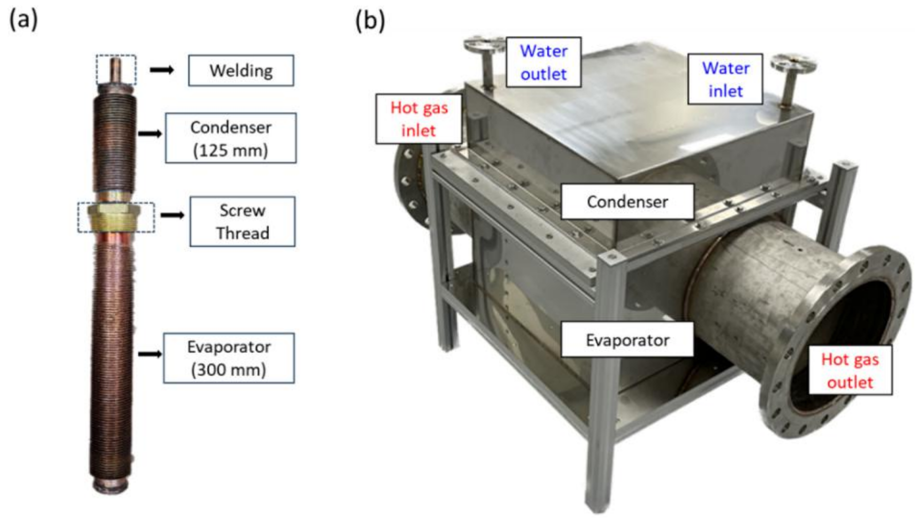

Fig. 4. **| Image of the HPHX.** (**a**) Finned heat pipe elements. (**b**) HPHX module.

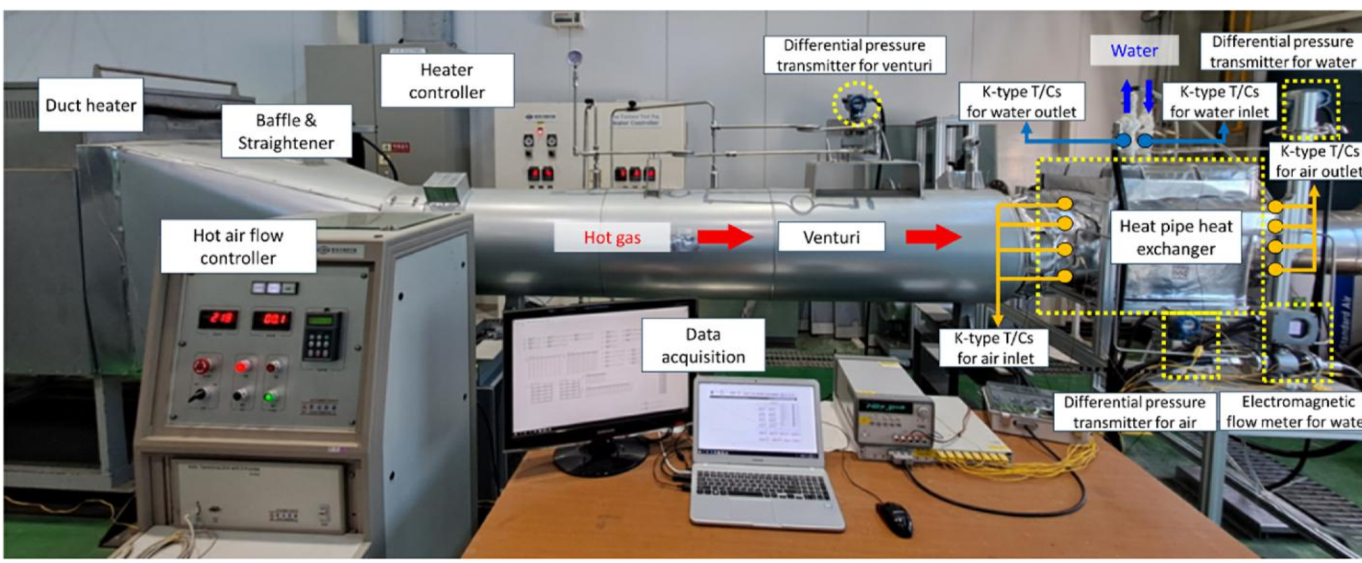

Fig. 5. **| Thermal testbed for evaluating HPHX thermal characteristics.** Preheated air (200 °C) was fed into the evaporator with flow rates ranging from 0.115 to 0.215 kg/s, measured by a venturi meter. Air temperatures at the inlet and outlet were recorded using K-type thermocouples. Water at 20 °C was supplied to the condenser with flow rates ranging from 0.106 to 0.190 kg/s, measured by an electromagnetic flowmeter. K-type thermocouples monitored water temperatures at both the inlet and outlet.

(Joul) before being directed into the evaporator by a blower. The air mass flow rate was recorded with a venturi meter, positioned upstream of the HPHX. The measurement of air flow rate is based on the pressure recorded using a Venturi (differential pressure transmitter, Honeywell, STD810). The design and measurement method for the Venturi adhere to the procedures outlined in ISO 5167-4 standard [39]. Four K-type thermocouples (OMEGA, KMTXL-062G-12) were strategically placed to measure the inlet and outlet temperatures of the evaporator. To ensure uniform temperature distribution and facilitate proper mixing of the hot air before entering the heat exchanger, four 10-mm thick stainless-steel baffles were installed between the heater and the venturi. These measures ensured exceptional temperature uniformity at the inlet, with a temperature variation of less than 1 °C. In the condenser, water was supplied at 20 °C from a tank, which was maintained at a constant temperature by an internal HPHX and an external chiller. The water mass flow rate was recorded using an electromagnetic flowmeter (TOSHIBA, LF630) before entering the HPHX, and the temperatures at both the inlet and outlet were monitored with K-type thermocouples (OMEGA, KMTXL-062G-12). To minimize heat loss during the tests, the entire exterior of the HPHX was insulated with fiberglass material. Temperatures, air mass flow rates, and water mass flow rates were all

Table 2
Parameters of the experimental setup.

No	Evaporator inlet		Condenser inlet	
	Mass flow rate [kg/s]	Temperature [°C]	Mass flow rate [kg/s]	Temperature [°C]
1	0.115	200	0.143	20
2	0.139			
3	0.165			
4	0.189			
5	0.215			
6	0.165		0.106	
7			0.124	
8			0.167	
9			0.190	

recorded using a data acquisition system (VTI, EX1032A). A summary of the experimental operating conditions is provided in Table 2. Each experiment was repeated at least three times to ensure setup accuracy and result consistency. The temperature, flow rate, and differential pressures measured in the repeated experiments exhibited consistent values with an error margin of less than 1 %. This repetitive testing approach ensured the reliability and precision of the data, reinforcing the robustness of the experimental design.

3.3. Experimental data reduction

The thermal performance of the HPHX was assessed by evaluating heat transfer rate and effectiveness. Temperature and flow rate data were measured over an average duration of 600-s under steady-state conditions. The heat transfer rate, Q, was calculated as the average of the heat transfer rates at the evaporator and condenser (Q_e and Q_c, respectively), determined as follows:

$$Q_e = \dot{m}_{air} c_{p,air} \left(T_{air,in} - T_{air,out}\right), \tag{5}$$

$$Q_c = \dot{m}_{w} c_{p,w} \left(T_{w,out} - T_{w,in}\right), \tag{6}$$

where $\dot{m}$ represents the mass flow rate, and c_p is the specific heat of the working fluid. The inlet and outlet fluid temperatures at the HPHX are denoted as T_{in} and T_{out}, respectively. The values for Q_e and Q_c were calculated based on the arithmetic average of the fluid temperatures measured at the HPHX's inlet and outlet.

The heat capacity rates of the air and water fluids in the evaporator and condenser sections (C_e and C_c) are defined as:

$$C_e = \dot{m}_{air} c_{p,air}, \tag{7}$$

$$C_c = \dot{m}_{w} c_{p,w}. \tag{8}$$

The effectiveness of the HPHX, ε, is defined as the ratio of Q to the maximum possible heat transfer rate, Q_{max}, shown as follows:

$$\varepsilon = \frac{Q}{Q_{max}}, \tag{9}$$

where Q_{max} is determined using the minimum heat capacity rate (C_{min}) between the air and water flows, along with the temperature difference at the inlets of both fluids:

$$Q_{max} = C_{min} \left(T_{air,in} - T_{w,in}\right). \tag{10}$$

The overall thermal resistance of the HPHX, R_{tot} (K/kW), can be calculated using the following equation:

$$R_{tot} = \frac{\Delta T_{LM}}{Q}, \tag{11}$$

where Q is the heat transfer rate and ΔT_{LM} is the logarithmic mean temperature difference between the inlet and outlet of the air and water streams. The logarithmic mean temperature difference, ΔT_{LM}, for a cross-flow heat exchanger is given by Ref. [40]:

$$\Delta T_{LM} = \left[\left(T_{air,in} - T_{water,out}\right) - \left(T_{air,out} - T_{water,in}\right)\right] \Big/ ln\left(\frac{T_{air,in} - T_{water,out}}{T_{air,out} - T_{water,in}}\right). \tag{12}$$

3.4. Uncertainty analysis

The uncertainty in the Q and ε was evaluated following the guidelines in the GUM [41]. The combined standard uncertainty (δf) was calculated as follows [42]:

$$\delta f = \sqrt{\sum_{i=1}^{n} \left(\frac{\delta f}{\delta x_i} \delta x_i\right)^2}, \tag{13}$$

where $\partial f / \partial x_i$ represents the sensitivity coefficient, and δx_i denotes the standard uncertainty of each independent variable. The experimental measurements for Q_e and Q_c showed an average discrepancy of 0.8 %, which was also observed in the measured values for ε_{evap} and ε_{cond}. The average relative uncertainties were 0.79 % for Q_e, 1.59 % for Q_c, and 1.20 % for ε. A summary of the calculated uncertainties for Q_e, Q_c, and ε is provided in Appendix C of the Supporting Information.

4. Results and discussion

A full-scale conjugate analysis was conducted to evaluate the energy-harvesting potential of the HPHX. A porous media modeling approach, incorporating LTNE effects, was employed to perform an in-depth heat transfer and fluid flow analysis across a broad spectrum of operating conditions. The highest-performing HPHX, as identified through the porous media analysis, was subsequently validated through extensive full-scale experimental testing.

4.1. Result analysis of LTE and LTNE at full scale

The performance was assessed using various thermal models within the porous medium during a comprehensive full-scale conjugate analysis. Figs. 6 and 7 illustrate the variations in heat transfer rate, effectiveness, fluid temperatures, and overall thermal resistance under LTE and LTNE conditions as a function of water and airflow rates.

Under LTE conditions, the total energy harvested ranged from 20.6 to 37.3 kW for air mass flow rates between 0.115 and 0.215 kg/s, and water mass flow rates between 0.106 and 0.190 kg/s. In contrast, under LTNE conditions, the energy harvesting capacity decreased to a range of 16.9–27.9 kW for the same flow rates. Additionally, the effectiveness was significantly higher under LTE conditions, ranging from 0.95 to 0.99, compared to 0.72 to 0.83 under LTNE conditions. This disparity arose because LTE assumes uniform temperatures across the solid and fluid phases within the porous media, resulting in an infinitely high heat transfer coefficient and thus overestimating heat transfer and effectiveness.

As shown in Fig. 6(a), under LTE conditions, the heat transfer rate increased substantially from 20.6 to 37.3 kW, reflecting an approximate 81 % increase as the air mass flow rate increased from 0.115 to 0.215 kg/s, with the water mass flow rate held constant at 0.143 kg/s. This increase is mainly attributed to improved convective heat transfer and reduced advective thermal resistance at higher air mass flow rates. In contrast, under LTNE conditions, as illustrated in the same figure, the heat transfer rate rose from 16.9 to 27.9 kW, a 65 % increase for the same flow rate variation. This is about 16 % lower than the increase observed under LTE conditions. The smaller rise under LTNE conditions can be explained by the finite heat transfer rate within the porous media, which moderates the effect of the increased air mass flow rate compared to the LTE scenario.

Fig. 6(b) shows that the heat transfer rate also increases as the water mass flow rate rises from 0.106 to 0.190 kg/s. Under LTE conditions, the heat transfer rate increased modestly from 28.4 to 29.8 kW, a 4.9 % rise. Under LTNE conditions, the heat transfer rate increased from 21.9 to 23.6 kW, a 7.7 % increase. While increased flow rates of both working fluids lead to higher heat transfer rates in the HPHX, the effect of changes in water flow rate is less pronounced than that of air mass flow rate changes. This is because water's high heat capacity reduces the influence of advective thermal resistance within the total thermal resistance, resulting in less variation in the heat transfer rate as water flow rates change.

Notably, the increase in heat transfer rate due to changes in the air mass flow rate was more significant under LTE conditions than under LTNE conditions. Conversely, variations in water mass flow rate resulted in a greater increase in heat transfer rate under LTNE conditions than under LTE conditions. This is primarily due to the larger increase in the

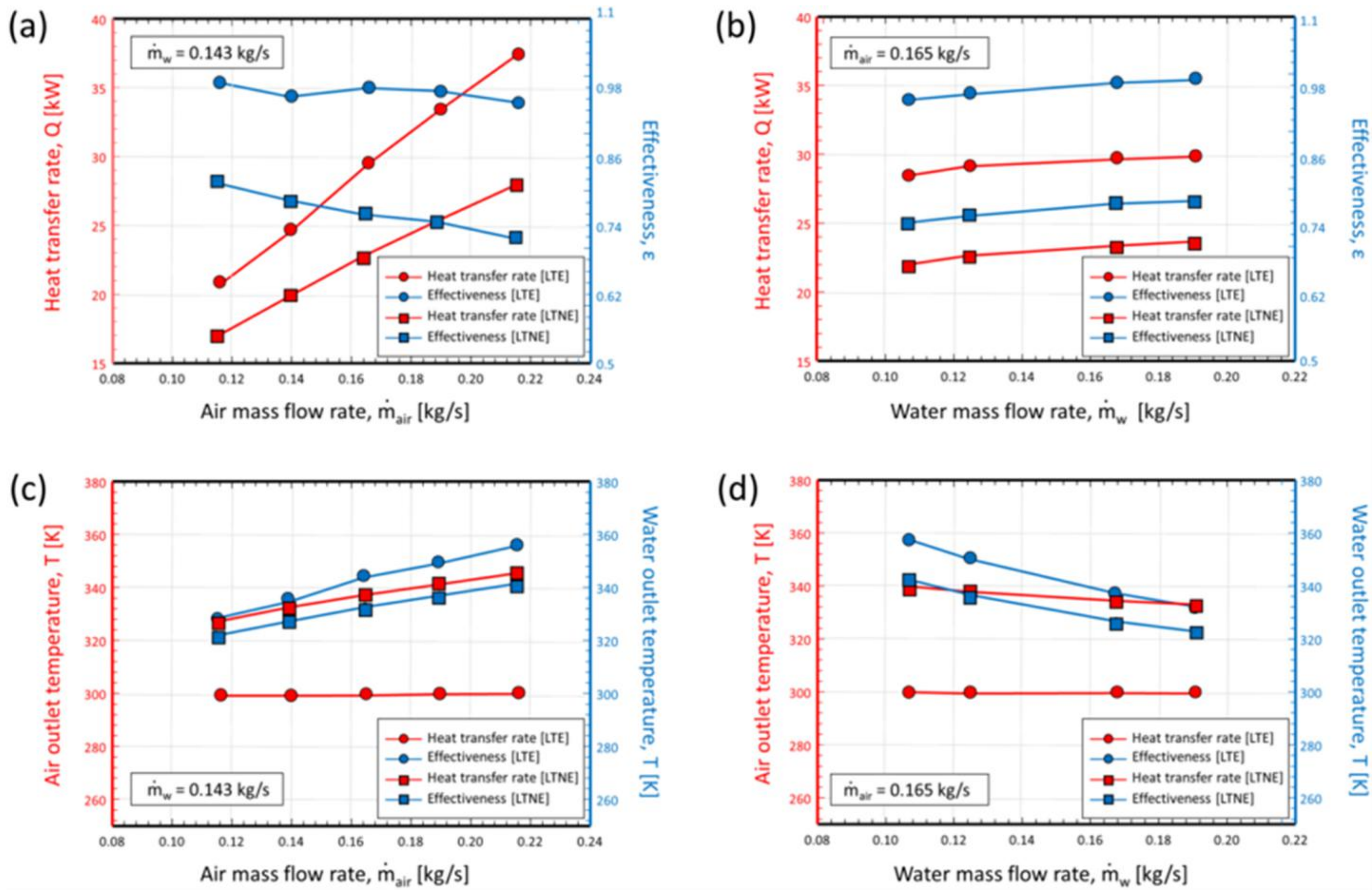

Fig. 6. | **Comparative analysis between LTNE and LTE.** (**a-b**) Heat transfer rate, effectiveness, and (**c-d**) outlet temperatures.

temperature differential between the inlet and outlet air under LTNE conditions, driven by higher water mass flow rates, compared to the corresponding changes under LTE conditions.

Under LTE conditions, the effectiveness slightly decreased from 0.99 to 0.95 as the air mass flow rate increased, while it increased from 0.95 to 0.99 with rising water flow rates. The decrease in effectiveness at higher air flow rates is attributed to an increase in heat capacity, which raises the maximum heat transfer rate, Q_{max}. However, as the airflow rate increased, the temperature difference between the inlet and outlet air decreased, leading to a reduction in the actual heat transfer rate, Q, and consequently a decrease in effectiveness. In contrast, as the water flow rate increased, the temperature difference between the inlet and outlet air widened, and since the rate of increase in Q exceeded that of Q_{max}, the effectiveness improved from 0.95 to 0.99.

Under LTNE conditions, the effectiveness decreased more significantly, from 0.81 to 0.72 as the air mass flow rate increased, but showed a modest increase from 0.77 to 0.83 with increasing water flow rates. This behavior can be explained by the lower heat capacity of air under LTNE conditions, which contrasts with the infinitely high HTC assumed under LTE conditions. As a result, LTE conditions exhibit a larger variation in the temperature difference between the inlet and outlet air with changes in flow rates, leading to a broader range of effectiveness changes compared to LTNE conditions.

Fig. 7 shows the total thermal resistance in the HPHX under both LTE and LTNE conditions. Under LTE conditions, increasing the air mass flow rate significantly reduced the overall thermal resistance from 2 to 0.9 K/kW. In contrast, increasing the water mass flow rate only caused slight fluctuations, with thermal resistance remaining relatively stable between 1.2 and 1.3 K/kW. The reduction in thermal resistance at higher air flow rates is primarily due to a decrease in forced convection resistance, which results from an increased Reynolds number on the evaporator side. The high heat capacity of water minimizes the influence of advective thermal resistance on the overall thermal resistance, causing less variation in heat transfer rates with changes in water flow rates. Consequently, air flow rate variations on the evaporator side have a more significant impact on thermal resistance and heat transfer than changes in water flow rate on the condenser side. Under LTNE conditions, increasing the air mass flow rate decreased the overall thermal resistance from 4.5 to 3 K/kW. However, under the same conditions, the thermal resistance only slightly decreased from 3.7 to 3.5 K/kW as the water mass flow rate increased. The higher thermal resistance observed under LTNE compared to LTE is due to the lower heat transfer coefficient in LTNE. The reduction in thermal resistance with increasing air mass flow rate under LTNE follows the same principle as under LTE: a reduction in forced convection resistance due to a higher Reynolds number. As with LTE, changes in the air mass flow rate on the evaporator side had a more pronounced effect on thermal resistance and heat transfer than changes in the water flow rate on the condenser side.

Fig. 8 compares the temperature and velocity contours between LTE and LTNE at the midpoint of the evaporator and condenser sections in a full-scale analysis. The analysis aimed to maximize the energy-harvesting capacity of the HPHX, with operational flow rates ranging from 0.115 to 0.215 kg/s for air and from 0.106 to 0.19 kg/s for water. The contour data was validated using reference flow rates of 0.165 kg/s for air and 0.143 kg/s for water.

The results showed that LTE, assuming thermal equilibrium, facilitated much faster heat exchange than LTNE. In LTE, the heat exchange was almost complete near the air inlet, while in LTNE, heat exchange occurred more uniformly along the flow path. Although the air inlet velocity was the same for both models (3.12 m/s), the overall average

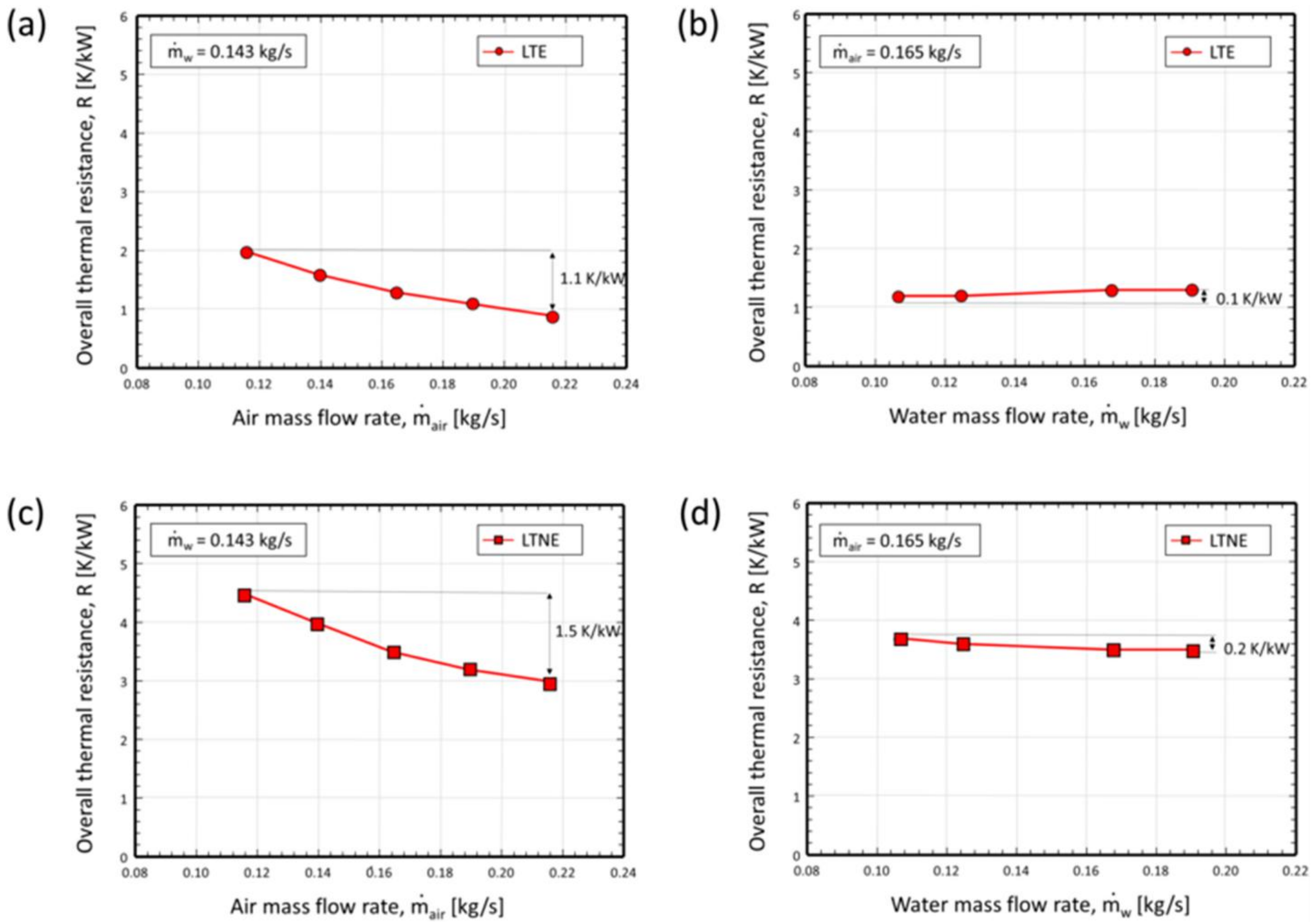

Fig. 7. | **Comparative analysis between LTNE and LTE.** (**a-b**) Overall thermal resistance in LTE for each fluid at different mass flow rates, and (**c-d**) overall thermal resistance in LTNE conditions.

velocity in LTE was 1.14 m/s slower, with a corresponding lower fluid temperature. Water, due to its significantly higher density than air, exhibited much lower velocity, leading to minimal differences in flow velocity between LTE and LTNE.

4.2. Experimental results

A full-scale HPHX was constructed, and its energy-harvesting performance was experimentally measured to validate the simulation results. The experimental validation was carried out using the same flow rates for the working fluids as those in the analysis.

Fig. 9 presents the experimentally measured HPHX performance. Fig. 9(a) shows the results for five different air mass flow rates, with the water mass flow rate held constant at 0.143 kg/s Fig. 9(b) illustrates the results for four different water mass flow rates, while the air mass flow rate was kept at 0.165 kg/s. Additionally, Fig. 9(c) and (d) display the outlet temperatures for air and water under each mass flow rate condition, respectively.

As the air mass flow rate increased from 0.115 to 0.215 kg/s, the heat transfer rate increased from 17.7 to 30.1 kW. As observed in the simulation analysis, the effectiveness decreased from 0.85 to 0.77. In Fig. 9 (a), with the water flow rate held constant, increasing the air mass flow rate enhances convective heat transfer and reduces advective thermal resistance, which leads to an increase in the heat transfer rate (Q). Due to the lower specific heat capacity of air, the minimum heat capacity (C_{min}) is always determined by the heat capacity of air (C_e). Consequently, as the air mass flow rate increases, heat transfer improves, and the maximum heat transfer rate (Q_{max}) also increases, as described in Equation (10). However, the increase in mass flow rate results in a reduced temperature difference between the inlet and outlet of the evaporator. Therefore, while Q_{max} increases, the reduction in the temperature difference outweighs this, leading to a decrease in effectiveness.

When the air mass flow rate is held constant, increasing the water mass flow rate from 0.106 to 0.19 kg/s results in a heat transfer rate increase from 23 to 25.3 kW. In this case, as in the simulation, effectiveness improves from 0.77 to 0.83 (Fig. 9(b)). When the air flow rate is held constant, the rise in the water mass flow rate leads to a slight increase in the heat transfer rate, as shown in Fig. 9(b). This is because the high heat capacity of water reduces the impact of fluid thermal resistance on the overall thermal resistance, thus minimizing variations in the heat transfer rate caused by changes in water flow rate. Unlike the air mass flow rate increase, which decreases effectiveness, the increase in water mass flow rate results in an improvement in effectiveness. This is because, with the air mass flow rate fixed, Q_{max} remains constant, while the temperature difference between the evaporator inlet and outlet increases, thereby enhancing effectiveness.

Fig. 9(c) and (d) show the changes in the outlet temperatures for air and water as the mass flow rates of both fluids vary. In Fig. 9(c), the air outlet temperature increases from 317.95 to 333.35 K due to the increase in air heat capacity, indicating a decrease in the temperature difference between the inlet and outlet. For water, the outlet temperature rises from 322.65 to 344.05 K as the water inlet temperature is 293.15 K. This demonstrates an increase in the temperature difference

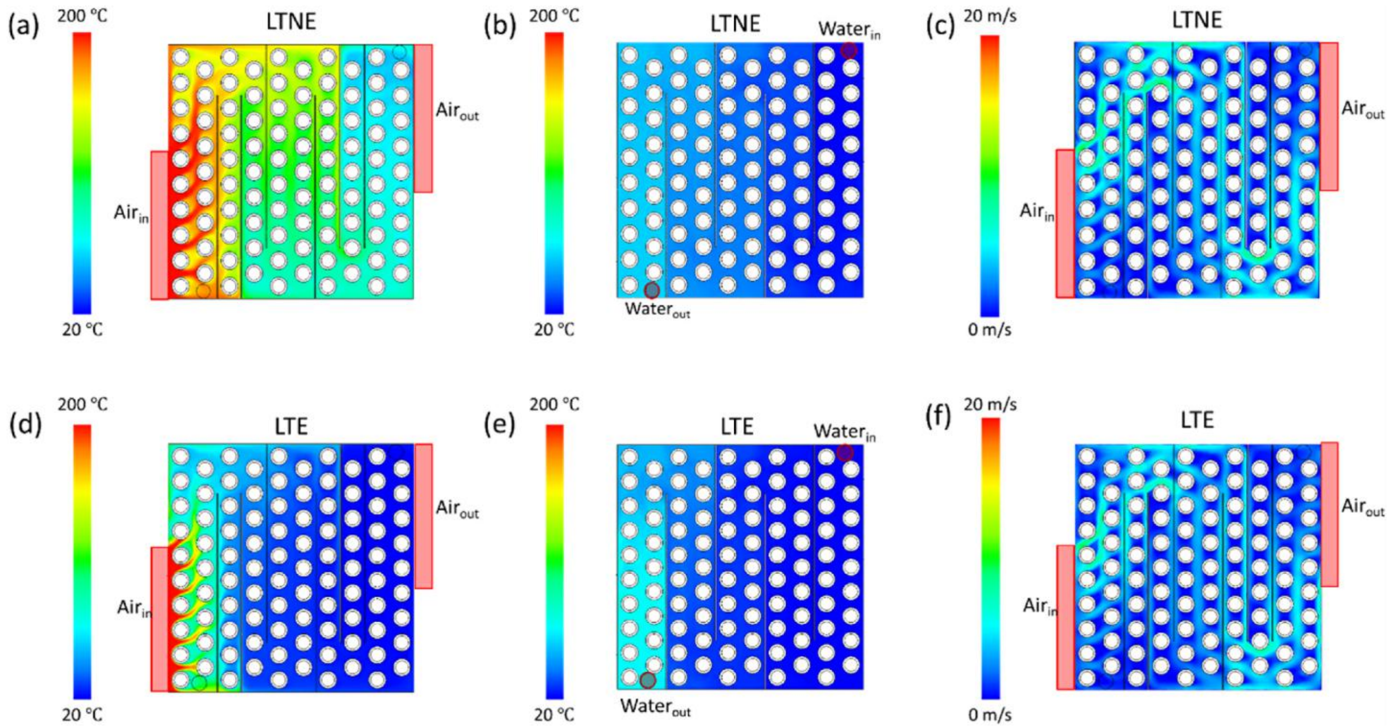

Fig. 8. **| Comparison of temperature and velocity contours between LTE and LTNE.** (**a**) and (**d**) Air temperatures in LTE and LTNE ($H_e/2 = 150$ mm). (**b**) and (**d**) Water temperatures in LTE and LTNE ($H_c/2 = 62.5$ mm). (**c**) and (**f**) Air velocities in LTE and LTNE ($H_e/2 = 150$ mm).

between the inlet and outlet, driven by the higher heat capacity of air.

Fig. 9(d) shows that as the water mass flow rate increased, the air outlet temperature decreased from 332.35 to 322.65 K, which corresponds to an increased temperature difference between the inlet and outlet. Conversely, the water outlet temperature decreased from 345.55 to 325.85 K, indicating a reduction in the temperature difference between the inlet and outlet.

As illustrated in Fig. 9(e), the overall thermal resistance significantly decreased from 3.8 to 2.4 K/kW as the air mass flow rate increased, consistent with the results from the analysis. In contrast, Fig. 9(f) shows that the overall thermal resistance remained nearly constant, varying only slightly from 3.2 to 2.8 K/kW as the water mass flow rate increased, which also aligns with the analysis findings. Experimentally, as in the analysis, it was confirmed that variations in mass flow rate on the evaporator side had a greater impact on the overall thermal resistance than changes on the condenser side.

4.3. Comparison of simulation results using LTE and LTNE with experimental data

The experimental results were comprehensively compared with the simulation outcomes from the LTE and LTNE models. Fig. 10 presents a comparison of heat transfer rate, effectiveness, and overall thermal resistance for different working fluid mass flow rates. Fig. 10(a), (b), and 10(c) compare the heat transfer rate, effectiveness, and overall thermal resistance for varying air mass flow rates, while Fig. 10(d), (e), and 10(f) show the corresponding results for varying water mass flow rates.

The LTE model, which assumes an infinite HTC, exhibited a greater variation in the heat transfer rate compared to the experimental data. Specifically, as the air mass flow rate increased from 0.115 kg/s to 0.215 kg/s, the heat transfer rate increased from 2.8 to 7.2 kW (a variation of 16 %–23.9 %). In contrast, LTNE showed much smaller discrepancies, with differences ranging from 0.79 to 2.1 kW (5 %–7.5 %) when compared to the experimental results.

For changes in water mass flow rate, the heat transfer rate difference between the experimental results and LTE ranged from 4.5 to 5.4 kW (17.9 %–21.9 %). LTNE, however, demonstrated a smaller error of 1–1.7 kW (5.1 %–7.2 %).

Both LTE and LTNE followed the same trend as the experimental results, with effectiveness decreasing as the air mass flow rate increased. However, LTE exhibited a higher error margin, with discrepancies ranging from 0.13 to 0.18 (15.5 %–23.3 %) compared to the experimental results. In contrast, LTNE showed a smaller error of 0.03–0.05 (5 %–7.2 %). For variations in water mass flow rate, LTE showed a larger effectiveness difference of 0.15–0.18 (18.5 %–23.2 %), while LTNE's error was smaller at 0.03 to 0.05 (4.6 %–6.8 %).

With respect to overall thermal resistance, the error between the experimental results and LTE was significant, ranging from 47 % to 62.5 %. LTNE, in contrast, displayed a much smaller error margin of 15 %–25 %. When compared to experimental data, LTE conditions exhibited a maximum average absolute percentage error of ±19.8 % in terms of heat transfer rate and effectiveness. In contrast, LTNE showed a closer alignment with the experimental data, with a maximum average absolute percentage error of ±6.2 %.

5. Conclusion

This study examined the thermal performance of a heat pipe heat exchanger (HPHX) with multiple fins. To simplify the finned section, a porous media model was used, representing the finned area as an annular porous medium. Two thermal models were assessed: the local thermal equilibrium model and the local thermal nonequilibrium model. Experimental results confirmed the predictive accuracy of both models. This analysis led to the successful development of an HPHX capable of recovering over 30 kW of waste heat, contributing to advancements in the design and efficiency of waste heat recovery systems:

(1) The energy harvesting capacity of the HPHX was assessed across a range of air and water mass flow rates (air: 0.115–0.215 kg/s, water: 0.106–0.19 kg/s). In the local thermal equilibrium model, the energy recovery increased from 20.6 kW to 37.3 kW as the air mass flow rate rose, and it increased from 28.4 kW to 29.8 kW

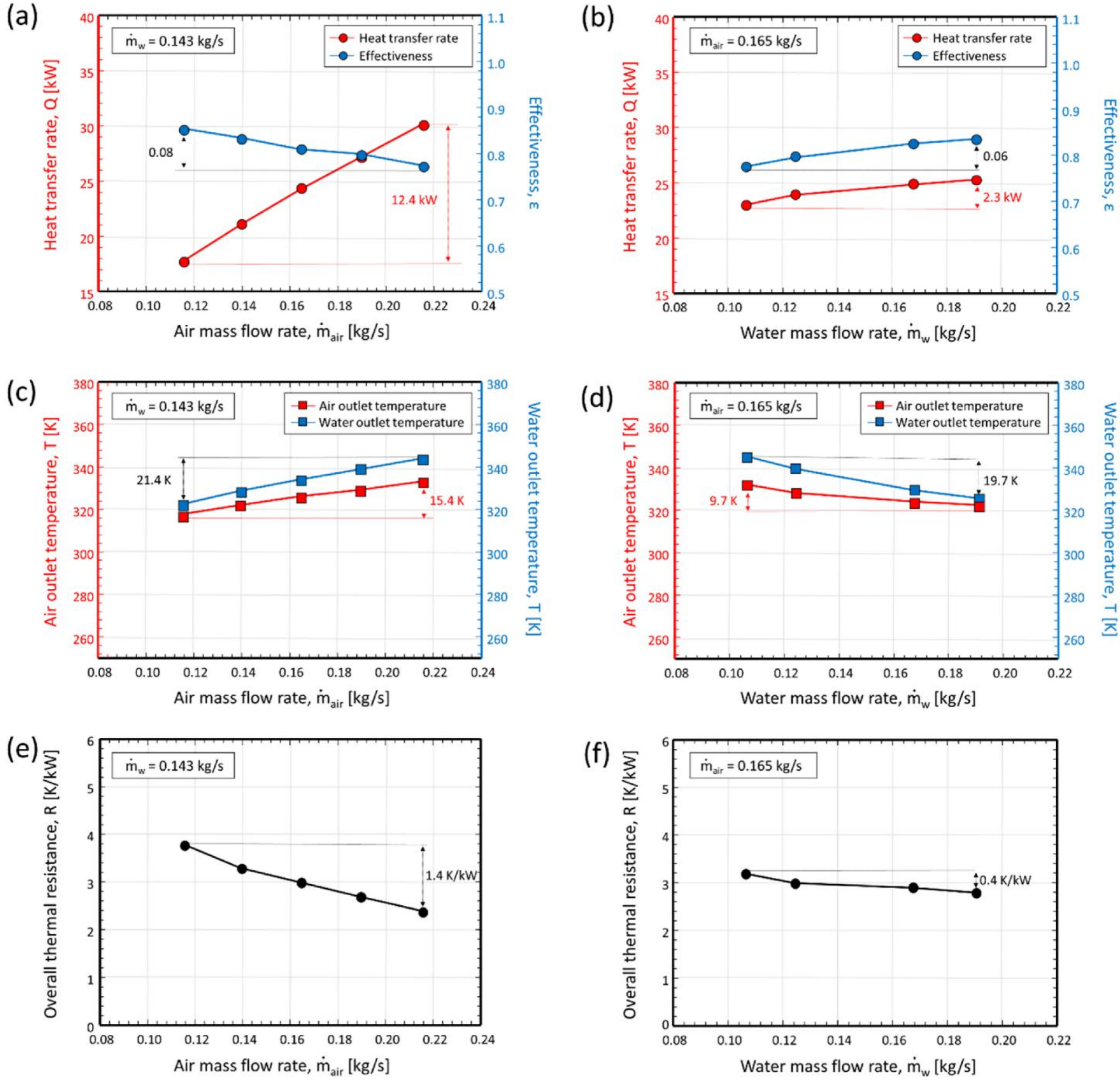

Fig. 9. | Experimental results for the HPHX. (**a-b**) Heat transfer rate and effectiveness, (**c-d**) Outlet temperature, and (**e-f**) Overall thermal resistance for each fluid at different fluid mass flow rates.

with rising water mass flow rates. In the local thermal nonequilibrium model, energy recovery varied from 16.9 kW to 27.9 kW with increasing air flow rates, and from 21.9 kW to 23.6 kW with increasing water flow rates. The effectiveness of the HPHX ranged from 0.95 to 0.99 in the local thermal equilibrium model and from 0.72 to 0.83 in the local thermal nonequilibrium model.

(2) Experimental results closely aligned with the analytical models. In experiments, energy recovery varied from 17.7 to 30.2 kW with increasing air flow rates, and from 23 to 25.3 kW with increasing water flow rates. The experimental effectiveness ranged from 0.73 to 0.85.

(3) A comparative analysis between the two models revealed that the local thermal nonequilibrium model was more accurate, with predictive errors for heat transfer rates ranging from 5 % to 7.5 % and for effectiveness ranging from 5.2 % to 8.3 %.

(4) The constructed HPHX successfully recovered 30.2 kW of waste heat with an efficiency of 0.78, and is expected to be suitable for a variety of industrial applications, including gas turbine exhaust systems, steel heat treatment processes, and organic chemical processing. This versatility underscores the potential of the HPHX to significantly enhance energy efficiency across multiple sectors.

CRediT authorship contribution statement

Seungjae Lee: Writing – original draft, Methodology, Investigation, Formal analysis, Data curation. **Sukkyung Kang:** Methodology, Investigation. **Yunseo Kim:** Investigation, Formal analysis. **Gyohoon Geum:**

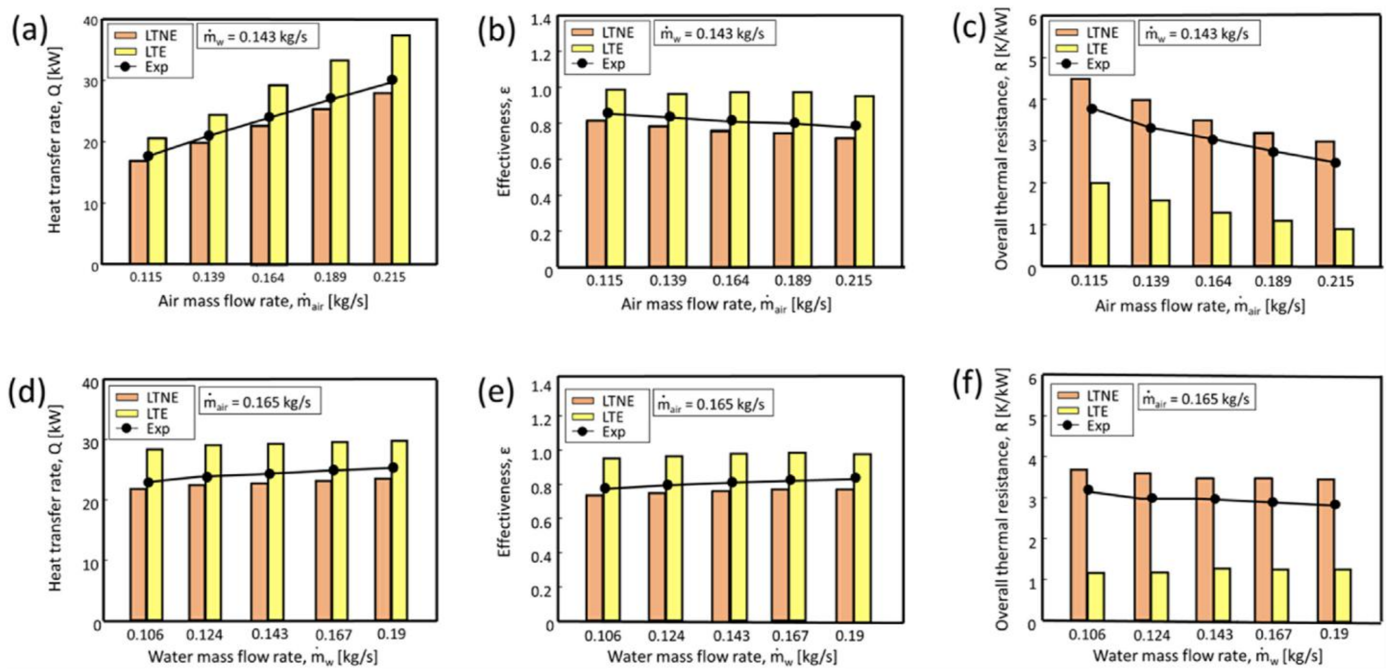

Fig. 10. | **Comparative analysis of LTNE, LTE, and experimental results.** The figures illustrate the (**a**) Heat transfer rate, (**b**) Effectiveness, and (**c**) Overall thermal resistance at various air mass flow rates. (**d**) Heat transfer rate, (**e**) Effectiveness, and (**f**) Overall thermal resistance at varying water mass flow rates.

Methodology, Investigation, Formal analysis. **Daeyoung Kong:** Methodology, Formal analysis. **Dong Hwan Shin:** Methodology, Investigation, Formal analysis. **Seong Hyuk Lee:** Writing – review & editing, Supervision, Project administration. **Jungho Lee:** Writing – review & editing, Supervision, Project administration, Funding acquisition. **Hyoungsoon Lee:** Writing – review & editing, Supervision, Project administration.

Declaration of competing interest

The authors declare that they have no known competing financial interests or personal relationships that could have appeared to influence the work reported in this paper.

Acknowledgments

This work was supported by the Korea Institute of Energy Technology Evaluation and Planning (KETEP) grant, funded by the Ministry of Trade, Industry, and Energy, Korea (Grant No. 20212020800270), the International Cooperative R&D Program of the Korea Institute of Energy Technology Evaluation and Planning (KETEP), a grant funded by the Ministry of Trade, Industry & Energy, Korea. (Grant No. RS-2024-00436521) and the Chung-Ang University Graduate Research Scholarship in 2023.

Appendix A. Supplementary data

Supplementary data to this article can be found online at https://doi.org/10.1016/j.energy.2025.134731.

Data availability

Data will be made available on request.

References

[1] Lee C-C, Zihao Y, Qiaoru W. How does information and communication technology affect energy security? International evidence. Energy Econ 2022;109:105969.
[2] Wang E-Z, Lee C-C. The impact of information communication technology on energy demand: some international evidence. Int Rev Econ Finance 2022;81:128–46.
[3] Dong K, Xiucheng D, Qingzhe J. How renewable energy consumption lower global CO_2 emissions? Evidence from countries with different income levels. World Econ 2020;43(6):1665–98.
[4] Lawrence Livermore National Laboratory. Energy flow charts: charting the complex relationships among energy, water, and carbon. https://flowcharts.llnl.gov/; 2022.
[5] Cullen JM, Julian MA. Theoretical efficiency limits for energy conversion devices. Energy 2010;35(5):2059–69.
[6] Abdelkareem MA, Maghrabie HM, Sayed ET, Kais ECA, Abo-Khalil AG, Al Radi M, Baroutaji A, Olabi AG. Heat pipe-based waste heat recovery systems: background and applications. Therm Sci Eng Prog 2022;29.
[7] Ahmadzadehtalatapeh M, Yau YH. The application of heat pipe heat exchangers to improve the air quality and reduce the energy consumption of the air conditioning system in a hospital ward - a full year model simulation. Energy Build 2011;43(9):2344–55.
[8] Srimuang W, Amatachaya P. A review of the applications of heat pipe heat exchangers for heat recovery. Renew Sustain Energy Rev 2012;16(6):4303–15.
[9] Jouhara H, et al. Experimental and theoretical investigation of a flat heat pipe heat exchanger for waste heat recovery in the steel industry. Energy 2017;141:1928–39.
[10] Zhuang J, Zhang H. Prospect of heat pipe technology for year 2010. Chemical Engineering and Machinery 1998;25:44–9.
[11] Zhang H, Jun Z. Research, development and industrial application of heat pipe technology in China. Appl Therm Eng 2003;23(9):1067–83.
[12] Yang F, Xiugan Y, Guiping L. Waste heat recovery using heat pipe heat exchanger for heating automobile using exhaust gas. Appl Therm Eng 2003;23(3):367–72.
[13] Wu XP, Peter J, Aliakbar A. Application of heat pipe heat exchangers to humidity control in air-conditioning systems. Appl Therm Eng 1997;17(6):561–8.
[14] Abd E-B, Mostafa A, Mousa MM. Heat pipe heat exchanger for heat recovery in air conditioning. Appl Therm Eng 2007;27(4):795–801.
[15] Longo GA, et al. Experimental and theoretical analysis of a heat pipe heat exchanger operating with a low global warming potential refrigerant. Appl Therm Eng 2014;65(1–2):361–8.
[16] Jouhara H, et al. Investigation on a full-scale heat pipe heat exchanger in the ceramics industry for waste heat recovery. Energy 2021;223:120037.
[17] Tan JO, Liu CY. Predicting the performance of a heat-pipe heat exchanger, using the effectiveness-NTU method. Int J Heat Fluid Flow 1990;11(4):376–9.
[18] Brough D, et al. Development and validation of a TRNSYS type to simulate heat pipe heat exchangers in transient applications of waste heat recovery. International Journal of Thermofluids 2021;9:100056.
[19] Mroue H, et al. Experimental and numerical investigation of an air-to-water heat pipe-based heat exchanger. Appl Therm Eng 2015;78:339–50.
[20] Cho S, et al. Experimental and computational investigation of thermal performance and fluid flow in two-phase closed thermosyphon. Appl Therm Eng 2023;235:121327.
[21] Brough D, et al. An experimental study and computational validation of waste heat recovery from a lab scale ceramic kiln using a vertical multi-pass heat pipe heat exchanger. Energy 2020;208:118325.

[22] Selma B, Martin D, Pierre P. Optimization of an industrial heat exchanger using an open-source CFD code. Appl Therm Eng 2014;69(1–2):241–50.
[23] Geum G, et al. Thermal performance analysis of heat pipe heat exchanger for effective waste heat recovery. Int Commun Heat Mass Tran 2024;151:107223.
[24] Ramos J, Alex C, Hussam J. Experimental and numerical investigation of a cross flow air-to-water heat pipe-based heat exchanger used in waste heat recovery. Int J Heat Mass Tran 2016;102:1267–81.
[25] Varol Y, Hakan FO, Asaf V. Effects of thin fin on natural convection in porous triangular enclosures. Int J Therm Sci 2007;46(10):1033–45.
[26] Lindqvist K, Erling N. A validated CFD model of plain and serrated fin-tube bundles. Appl Therm Eng 2018;143:72–9.
[27] Qu T, et al. Multiscale simulations of fluid flow for finned elliptic tube heat exchangers using porous media approach. In: ASME international mechanical engineering congress and exposition, vol. 46552. American Society of Mechanical Engineers; 2014.
[28] Güler KG. Computational modeling of fin-and-tube type vehicle radiators based on porous medium approach. MS thesis. Middle East Technical University; 2014.
[29] Gangapatnam P, Renju K, Venkateshan SP. Numerical simulation of heat transfer in metal foams. Heat Mass Tran 2018;54:553–62.
[30] Hayes AM, et al. The thermal modeling of a matrix heat exchanger using a porous medium and the thermal nonequilibrium model. Int J Therm Sci 2008;47(10):1306–15.
[31] Garofalo E, et al. Waste heat to power: technologies, current applications, and future potential. Energy Technol 2020;8(11):2000413.
[32] Kim Y, et al. Boiling and condensation heat transfer of inclined two-phase closed thermosyphon with various filling ratios. Appl Therm Eng 2018;145:328–42.
[33] Ramos J, Alex C, Hussam J. Experimental and numerical investigation of a cross flow air-to-water heat pipe-based heat exchanger used in waste heat recovery. Int J Heat Mass Tran 2016;102:1267–81.
[34] Lin W, et al. Comparison and analysis of heat transfer in aluminum foam using local thermal equilibrium or nonequilibrium model. Heat Tran Eng 2016;37(3–4):314–22.
[35] Li Z-Z, et al. An approach based on the porous media model for numerical simulation of 3D finned-tubes heat exchanger. Int J Heat Mass Tran 2021;173:121226.
[36] Bergman TL. Fundamentals of heat and mass transfer 7th. 2011.
[37] Guichet V, Sulaiman A, Hussam J. Nucleate pool boiling heat transfer in wickless heat pipes (two-phase closed thermosyphons): a critical review of correlations. Therm Sci Eng Prog 2019;13:100384.
[38] Seo J, Shin D, Lee J. Study on working fluid filling into heat pipe by induction heating. The KSFM Journal of Fluid Machinery 2022;25(4):39–49.
[39] ISO 5167-4. Measurement of fluid flow by means of pressure differential devices inserted in circular cross-section conduits running full — Part 4: venturi tubes. International Standard Organization; 2003.
[40] Jouhara Hussam, et al. Experimental and theoretical investigation of the performance of an air to water multi-pass heat pipe-based heat exchanger. Energy 2021;219:119624.
[41] Joint Committee For Guides In Measurements. Guide to the expression of uncertainty in measurement 50. International Organization for Standardization Geneva; 2008. http://www.bipm.org/en/publications/guides/gum.html.
[42] Seo JinHyeuk, et al. Compact heat pipe heat exchanger for waste heat recovery within a low-temperature range. Int Commun Heat Mass Tran 2024;155:107550.